Input/Output Current Ripple Cancellation and RHP Zero Elimination in a Boost Converter using an Integrated Magnetic Technique

Yu Gu, *Student Member, IEEE*, Donglai Zhang, *Member, IEEE*, and Zhongyang Zhao

***Abstract*—This paper presents a novel integrated magnetic boost converter (IMBC) with both input/output current ripple cancellation and right-half-plane (RHP) zero elimination. The input inductor, output inductor, and the ripple cancellation network auxiliary inductor of the proposed IMBC have been integrated in one magnetic core. Two extra capacitors were added to achieve input and output current ripple cancellation. Therefore, the input current ripple of the IMBC dropped to one-twelfth of the original in a conventional boost converter, and the output current worked in continuous-conduction-mode with very small ripple. Meanwhile, the proposed IMBC has eliminated the RHP zero of the boost converter, which means higher bandwidth can be reached. The using of the integrated magnetic technique not only performs above advantages but also shows great potential for reducing the weight and volume of dc–dc converter. Finally, three 36 V input, 50 V output and 500 W prototypes operating at 100 kHz are implemented to verify the expected performance. The experimental results show that the proposed IMBC can achieve both input and output current ripple cancellation and RHP zero elimination with the maximum efficiency of 96.8%. All these advantages of the IMBC are very important especially in high dynamic response, high efficiency, and high-power application.**

***Index Terms*—Boost converter, integrated magnetic technique, right-half-plane zero, ripple cancellation.**

I. Introduction

THE conventional boost converters (CBC) are widely used in nonisolated applications. However, the small-signal control-to-output transfer function of CBC under continuous-conduction-mode has a well known right-half-plane (RHP) zero, which makes the CBC a nonminimum phase system with relatively low bandwidth and slow dynamic performance [1]. Although the discontinuous-conduction-mode CBC does not have RHP zero problem, the discontinuous input current increase the current stresses of the main switches and deteriorate the EMI characteristics [2]–[4].

Manuscript received November 12, 2013; revised January 16, 2014; accepted February 19, 2014. Date of publication February 26, 2014; date of current version October 7, 2014. This work was supported by the National Nature Science Foundation of China under Grant 51247009 and the International Science and Technology Cooperation Program of China under Grant 2010DFB63050. Recommended for publication by Associate Editor G. Moschopoulos.

The authors are with the Power Electronic and Motion Control Research Center, Shenzhen Graduate School of Harbin Institute of Technology, Shenzhen 518055, China (e-mail: zhangdl@hitsz.edu.cn).

Color versions of one or more of the figures in this paper are available online at http://ieeexplore.ieee.org.

Digital Object Identifier 10.1109/TPEL.2014.2307571

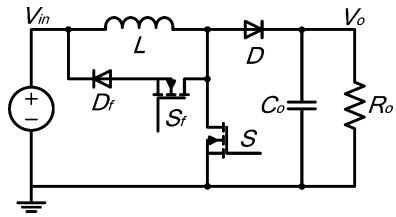

Fig. 1. Schematic of the tristate boost converter.

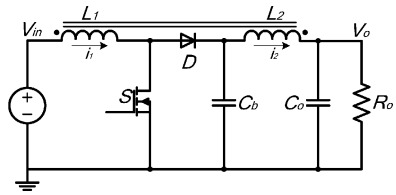

Fig. 2. Schematic of the boost converter with coupled LC filter.

The tristate boost converter with an auxiliary branch was proposed earlier in [5] and [6] to eliminate the RHP zero that occurs in the control-to-output transfer function of the CBC. The schematic of the tristate boost converter can be found in Fig. 1. The additional degree of freedom introduced in the converter in the form of a freewheeling interval has been exploited through a special control technique to achieve. However, adding of the extra switch and diode increase not only the cost and the losses, but also the controlling the complexity of the converter.

Magnetically coupling the input inductor and the output filter inductor of the CBC also known as boost converter with coupled *LC* filter (BCCF) has been proposed in [7] and [8] and shown in Fig. 2. It can be found that the magnetic coupling between two inductors transforms the original RHP zero into two zeros that can be located either in the right half-plane or left half-plane depending on the parameter values. However, the coupled inductors amplify the input current ripple and the current stresses of the converter and deteriorate the quality of input power supply. These drawbacks are almost fatal especially in large current applications [9].

The input current ripple of the CBC is inversely proportional to its input inductance value [10], which means that a large inductance value will result in a low input current ripple. However, the large inductance value increases the weight and volume of the converter. The coupled inductor can be applied to low-ripple dc–dc converter design [11] and the corresponding boost applications can be found in [12]–[16]. However, the challenging RHP zero problems still remained.

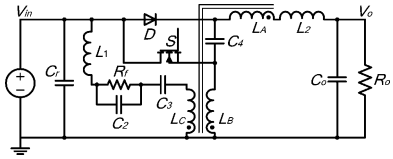

Fig. 3. Schematic of the multitapped inductor boost converter.

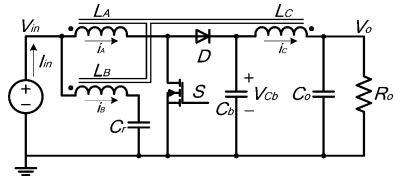

Fig. 4. Schematic of the proposed IMBC.

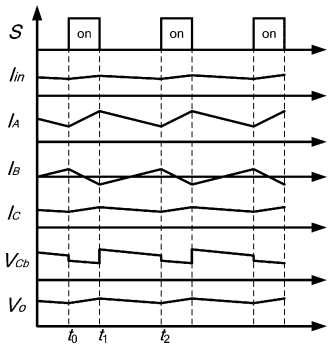

Fig. 5. Key waveforms of the proposed IMBC.

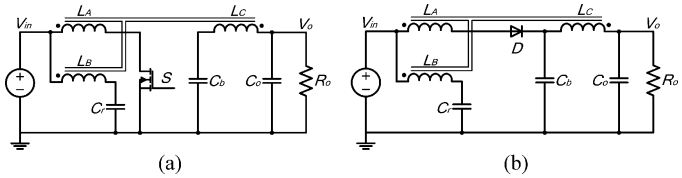

Fig. 6. Operation stages of the proposed IMBC. (a) Stage 1 $[t_0$–$t_1]$. (b) Stage 2 $[t_1$–$t_2]$.

A new boost-derived topology as shown in Fig. 3, multitapped inductor boost with ripple cancellation network, was proposed in [17] and [18]. The applications in [19]–[21] show that the proposed converter has several advantages over the CBC. However, the complex main structure with unwelcome RHP zero of this topology causes it unsuitable for high dynamic response applications.

According to statistics, the magnetic components generally occupy about 30–40% weight and 20–30% volume of the dc–dc converter, the proportion will be higher in some special applications [22], [23]. Since the high-power density and high-efficiency converter is limited by not only the weight and volume but also the number of the magnetic components, the magnetic path analyze and design has been an important factor in a dc–dc converter design process.

An integrated magnetic technique means to integrate all the magnetic components in one core, in order to reduce the weight, volume, and improve the dynamic performance [24]–[28]. A zero-voltage switching two-inductor boost converter with integrated magnetic is proposed in [29]. It utilizes one magnetic core and three winding coils to implement the two inductors and one transformer, the transformer leakage inductance functions as the resonant inductance. It has several advantages in the number of magnetic components and total volume. In the paper [30], a new buck-cascaded two-inductor boost converter and its integrated magnetic implementation are presented. It retains the main advantages of the buck-cascaded current-fed push–pull converter. The integration of the transformer and the inductors into a single magnetic structure using the integrated magnetic scheme, achieves several advantages such as reduced cure size, reduced ac flux ripple, improved filtering inductance, and continuous output current. A novel single-stage push–pull boost converter with an improved integrated magnetic and ripple-free input current is proposed in [31]. The presented converter can achieve smaller converter size and zero-input current using coupled inductor techniques, makes the conduction and switching losses low and may result in a high efficiency.

In this study, an integrated magnetic boost converter (IMBC) with input and output current ripple cancellation and RHP zero elimination has been proposed. The input current ripple cancellation network includes a capacitor and a coupled inductor which shares the same core with the main inductor and output inductor. The proposed integrated magnetic technique not only reduces the input and output current ripples but also solves the RHP zero problem of CBC. Meanwhile, the comparative experiment shows the weight and volume of the proposed IMBC can be minimized by using the integrated magnetic. In Section II, the operation analysis of the proposed IMBC is presented, and in Section III, the small-signal analysis of the BCCF and proposed IMBC are given. The simulation and experimental results of three 500 W prototypes are demonstrated in Sections IV and V. Finally, the paper is summarized and concluded in Section VI.

II. Proposed Converter and Operational Principle

The schematic of the proposed IMBC is shown in Fig. 4. Compared with the CBC, the input inductor has been replaced by an integrated magnetic component which includes the input inductor L_A, the auxiliary inductor L_B, and the output inductor L_C. Two extra capacitors C_r and C_b have been added to achieve ripple cancellation and RHP elimination. Other power components such as MOSFET S, diode *D,* and output capacitor C_o can also be found in the CBC.

The key steady waveforms of the proposed IMBC are depicted in Fig. 5. There are two stages in one operational period and the corresponding equivalent circuits for each operational stage are shown in Fig. 6.

Stage 1 [t_0, t_1]: The main switch S turns ON at t_0. The input inductor L_A is charged linearly by the input voltage, causing its current I_A increase linearly. The output diode D maintains OFF with the voltage stress equivalent to the output voltage $V_{\rm out}$. Because of the coupled relation between the input inductor L_A and auxiliary inductor L_B, the current ripple of the I_B shows opposite slope of the I_A and the average value of the I_B remains zero. That means the zero input current ripple can be achieved. Meanwhile, the output inductor current I_C starts

to increase linearly instead of decrease due to the prescribed coupled direction with the input inductor and causes the voltage of the buffer capacitor V_{Cb} decrease linearly. The integrated magnetic core current changing the rate of proposed IMBC during the main switch on-state can be expressed as differential (1)–(3), where $L_{\rm IMBC} = L_A L_B L_C - L_A M_{\rm BC}^2 - L_B M_{\rm AC}^2 - L_C M_{\rm AB}^2 + 2M_{\rm AB}M_{\rm AC}M_{\rm BC}$

$$\frac{di_A}{dt} = \frac{\left(L_B L_C - M_{\rm BC}^2\right)\cdot V_{\rm in}}{L_{\rm IMBC}} \tag{1}$$

$$\frac{di_B}{dt} = \frac{\left(M_{\rm BC}M_{\rm AC} - L_C M_{\rm AB}\right)\cdot V_{\rm in}}{L_{\rm IMBC}} \tag{2}$$

$$\frac{di_C}{dt} = \frac{\left(L_B M_{\rm AC} - M_{\rm AB}M_{\rm BC}\right)\cdot V_{\rm in}}{L_{\rm IMBC}}. \tag{3}$$

Stage 2 [t_1, t_2]: At t_1, the main switch S turns OFF. The energy stored in the input inductor L_A starts to transfer to the load R_o, causing the current I_A decrease linearly. The voltage stress of the switch S is equal to the output voltage $V_{\rm out}$. The auxiliary inductor current I_B still shows opposite slope of the I_A which can minimize the input current ripple. At the same time, the output inductor current I_C decrease linearly causing the buffer capacitor voltage V_{Cb} decrease linearly too. However, the capacitor C_b has been charged quickly at the t_1 moment, which ensures that there are enough energy stores in the C_b to be released in one entire switching cycle. The integrated magnetic core current changing the rate of the proposed IMBC during the main switch off-state can be expressed as differential equations given as follows:

$$\frac{di_A}{dt} = \frac{\left(L_B L_C - M_{\rm BC}^2\right)\cdot (V_{\rm in} - V_{\rm out})}{L_{\rm IMBC}} \tag{4}$$

$$\frac{di_B}{dt} = \frac{\left(M_{\rm BC}M_{\rm AC} - L_C M_{\rm AB}\right)\cdot (V_{\rm in} - V_{\rm out})}{L_{\rm IMBC}} \tag{5}$$

$$\frac{di_C}{dt} = \frac{\left(L_B M_{\rm AC} - M_{\rm AB}M_{\rm BC}\right)\cdot (V_{\rm in} - V_{\rm out})}{L_{\rm IMBC}}. \tag{6}$$

The input and output current ripple expressions of the proposed IMBC can be calculated from (1)–(6) and expressed as follows:

$$Di_{\rm in} = \frac{\left(L_B L_C - M_{\rm BC}^2 + M_{\rm AC}M_{\rm BC} - L_C M_{\rm AB}\right)\cdot V_{\rm in}\cdot D\cdot T}{L_{\rm IMBC}} \tag{7}$$

$$Di_{\rm out} = \frac{\left(L_B M_{\rm AC} - M_{\rm AB}M_{\rm BC}\right)\cdot V_{\rm in}\cdot D\cdot T}{L_{\rm IMBC}} \tag{8}$$

where the $M_{\rm AB} = k_{\rm AB}\sqrt{L_A L_B}$, $M_{\rm AC} = k_{\rm AC}\sqrt{L_A L_C}$, and $M_{\rm BC} = k_{\rm BC}\sqrt{L_B L_C}$.

Therefore, the input and output current ripple of the proposed converter can be minimized when the proper parameters have been chosen. By means of analysis, the input current ripple was only affected by the input inductor L_A and the ripple inductor L_B, meanwhile the output current ripple was only affected by the ripple inductor L_B and output inductor L_C. With the selected input inductance, the output inductance can be calculated to eliminate the RHP zero as shown in the next Section. After that, the ripple cancellation inductor winding can be integrated into the magnetic core to reduce the current ripple. Furthermore, the changing of the input voltage has minor influence on the input and output current ripples. According to the step-up ratio of the CBC, $V_{\rm in}\cdot D$ equal to $V_{\rm out}\cdot(1-D)\cdot D$. That means the maximal value of the IMBC input and output current ripples will appear when duty cycle $D = 0.5$.

As we know, the synchronous rectifier switch or output diode connected between the actual L (main inductor) and C (output capacitor) of the CBC is what is ultimately responsible for creating the RHP zero. Since it is virtually impossible to compensate the RHP zero in the boost converter by normal feedback control technique, we need to reduce the bandwidth of the converter open-loop gain plot to guarantee the crossover frequency must be set much lower than the location of this RHP zero. This results in a restricted closed-loop bandwidth (usually 1/30th of the switching frequency). Therefore, compared to the typical second-order conventional buck converters with minimum phase transfer functions, boost converters have relatively worse dynamic performance.

The previous figures and equations indicated that the integrated magnetic technique can ensure the output current of the proposed IMBC increases linearly and keeps continuously instead of equal to zero like the CBC when the main switch turns ON. When the duty cycle steps in the CBC, more energy is stored in the input inductor, rather than being sent to the output load, leading the output voltage initially decreases. However, the coupled relation between input inductor L_A and output inductor L_C of the proposed IMBC allows the energy being transferred to the output load even if the output diode turns off. Generally speaking, the additional energy channel provided by the integrated magnetic technique explains the physical principle of the RHP zero elimination. The detailed small-signal analysis can be found in the next Section.

III. Small-Signal Modeling and Analysis of the Proposed Converter

In order to achieve the small-signal analysis of the proposed IMBC, the analysis of the BCCF shown in Fig. 2 is given first. If we assume that the converter works in continuous mode, the switching frequency is much higher than the converter natural frequencies and no parasitic effects. The following differential equations can be derived after using the state space averaging method:

$$\begin{aligned}
\frac{d\bar{i}_{L1}}{dt} &= \frac{(\bar{v}_{Cb} - \bar{v}_o)M + (\bar{v}_{\rm in} - \bar{v}_{Cb} + \bar{v}_{Cb}d)L_2}{L_1L_2 - M^2}\\
\frac{d\bar{i}_{L2}}{dt} &= \frac{(\bar{v}_{Cb} - \bar{v}_o)L_1 + (\bar{v}_{\rm in} - \bar{v}_{Cb} + \bar{v}_{Cb}d)M}{L_1L_2 - M^2}\\
\frac{d\bar{v}_{Cb}}{dt} &= \frac{\bar{i}_{L1} - \bar{i}_{L2} - \bar{i}_{L1}d}{C_b}\\
\frac{d\bar{v}_o}{dt} &= \frac{\bar{i}_{L2}R_o - \bar{v}_o}{C_oR_o}
\end{aligned} \tag{9}$$

where d is the converter duty cycle and the superscript ($^-$) stands for the average value of the state variable in one switching cycle.

Linearizing the set of (9) around the equilibrium point leads to the small signal model, and the following control-to-output transfer function can be derived

$$G(s) = \frac{\hat{V}_o(s)}{\hat{d}(s)} = \frac{s^2 + a_1 s + a_0}{b_4 s^4 + b_3 s^3 + b_2 s^2 + b_1 s + b_0}. \quad (10)$$

The numerator coefficients are

$$a_1 = \frac{(1-D)M - L_1}{C_b M R_o (1-D)}, a_0 = \frac{1-D}{C_b M}. \quad (11)$$

Therefore, the BCCF will be a minimum phase system if the following condition is fulfilled:

$$\frac{M}{L_1} > \frac{1}{1-D}. \quad (12)$$

However, the adding of the coupled *LC* filter not only eliminates the RHP zero of the CBC but also increases its input current ripple. The input current ripples of the CBC and BCCF can be expressed as

$$\begin{aligned} Di_{\text{in-CBC}} &= \frac{V_{\text{in}}}{L_1} \cdot D \cdot T \\ Di_{\text{in-BCCF}} &= \frac{V_{\text{in}}}{L_1 (1-k^2)} \cdot D \cdot T. \end{aligned} \quad (13)$$

The k is the coupling coefficient of the coupled inductor. If k tends to one, the input current ripple approaches infinity. However, if k tends to zero, the output inductor value should be infinity to achieve RHP zero elimination. Therefore, an intermediate value of k is given by

$$k = \frac{1}{\sqrt{2}}. \quad (14)$$

The selected value of k also means the input current ripple of the BCCF has been doubled, when comparing with the CBC.

The differential equations of the proposed IMBC which shows in Fig. 4 can be derived after using the state space averaging method and shown in (15). The d is the converter duty cycle and the superscript ( ) stands for the average value of the state variable in one switching cycle

$$\begin{aligned} & L_A \frac{d\bar{i}_A}{dt} + M_{\text{AB}} \frac{d\bar{i}_B}{dt} - M_{\text{AC}} \frac{d\bar{i}_C}{dt} = \bar{v}_{\text{in}} - \left(1-\bar{d}\right) \bar{v}_{Cb} \\ & M_{\text{AB}} \frac{d\bar{i}_A}{dt} + L_B \frac{d\bar{i}_B}{dt} - M_{\text{BC}} \frac{d\bar{i}_C}{dt} = \bar{v}_{\text{in}} - \bar{v}_{Cr} \\ & - M_{\text{AC}} \frac{d\bar{i}_A}{dt} - M_{\text{BC}} \frac{d\bar{i}_B}{dt} + L_C \frac{d\bar{i}_C}{dt} = \bar{v}_{Cb} - \bar{v}_o \\ & C_r \frac{d\bar{v}_{Cr}}{dt} = \bar{i}_B \\ & C_b \frac{d\bar{v}_{Cb}}{dt} = \left(1-\bar{d}\right) \bar{i}_A - \bar{i}_C \\ & C_o \frac{d\bar{v}_o}{dt} = \bar{i}_C - \frac{\bar{v}_o}{R_o}. \end{aligned} \quad (15)$$

Likewise, after linearizing the set of (15) around the equilibrium point, the control-to-output transfer function of proposed IMBC can be derived as follows:

$$\begin{aligned} G(s)_{\text{IMBC}} &= \frac{\hat{V}_o(s)}{\hat{d}(s)} \\ &= \frac{a_4 s^4 + a_3 s^3 + a_2 s^2 + a_1 s + a_0}{b_6 s^6 + b_5 s^5 + b_4 s^4 + b_3 s^3 + b_2 s^2 + b_1 s + b_0}. \end{aligned} \quad (16)$$

After sorting and simplifying the expressions, the numerator coefficients are

$$\begin{aligned} a_4 &= C_b C_r C_o \left(L_B M_{\text{AC}} - M_{\text{AB}} M_{\text{BC}}\right) \\ a_3 &= \frac{C_r \left(L_B M_{\text{AC}} - M_{\text{AB}} M_{\text{BC}} + M_{\text{AB}}^2 - L_A L_B\right)}{R_o (1-D)} \\ a_2 &= C_b M_{\text{AC}} + C_r L_B \\ a_1 &= \frac{(1-D) M_{\text{AC}} - L_A}{R_o (1-D)} \\ a_0 &= (1-D) \end{aligned} \quad (17)$$

where the $M_{\text{AB}} = k_{\text{AB}} \sqrt{L_A L_B}$, $M_{\text{AC}} = k_{\text{AC}} \sqrt{L_A L_C}$, and $M_{\text{BC}} = k_{\text{BC}} \sqrt{L_B L_C}$.

Applying the Routh-Hurtwitz criterion to the numerator polynomial of (17), the following conditions ensuring the RHP zero elimination are derived

$$k_{\text{AC}} > k_{\text{AB}} \cdot k_{\text{BC}} \sqrt{\frac{L_C}{L_A}} > \frac{1 - k_{\text{AB}}^2}{k_{\text{AC}} - k_{\text{AB}} \cdot k_{\text{BC}}}. \quad (18)$$

Base on the previous selection of the coupling coefficient k, the intermediate values have been chosen for all three coupling coefficients of the proposed IMBC

$$k_{\text{AB}} = k_{\text{AC}} = k_{\text{BC}} = \frac{1}{\sqrt{2}}. \quad (19)$$

To compare with the CBC and BCCF, the key parameters of all three converters including proposed IMBC are chose and listed in Table I.

TABLE I
KEY PARAMETERS OF THE CONVERTERS

Basic Parameters	CBC	BCCF	IMBC
Input Voltage V_{in} (V)	36	36	36
Output Voltage V_{out} (V)	50	50	50
Output Power P_{out} (W)	500	500	500
Switching Frequency (kHz)	100	100	100
Input Inductor L_{A} (μH)	57.5	57.5	57.5
Ripple Inductor L_{B} (μH)	—	—	9.8
Output Inductor L_{C} (μH)	—	351.2	351.2
Coupling Coefficient k_{AB}	—	—	0.698
Coupling Coefficient k_{BC}	—	—	0.714
Coupling Coefficient k_{AC}	—	0.707	0.707
Capacitor C_{r} (μF)	—	—	10
Capacitor C_{b} (μF)	—	100	100
Output Capacitor C_{o} (μF)	470	470	470

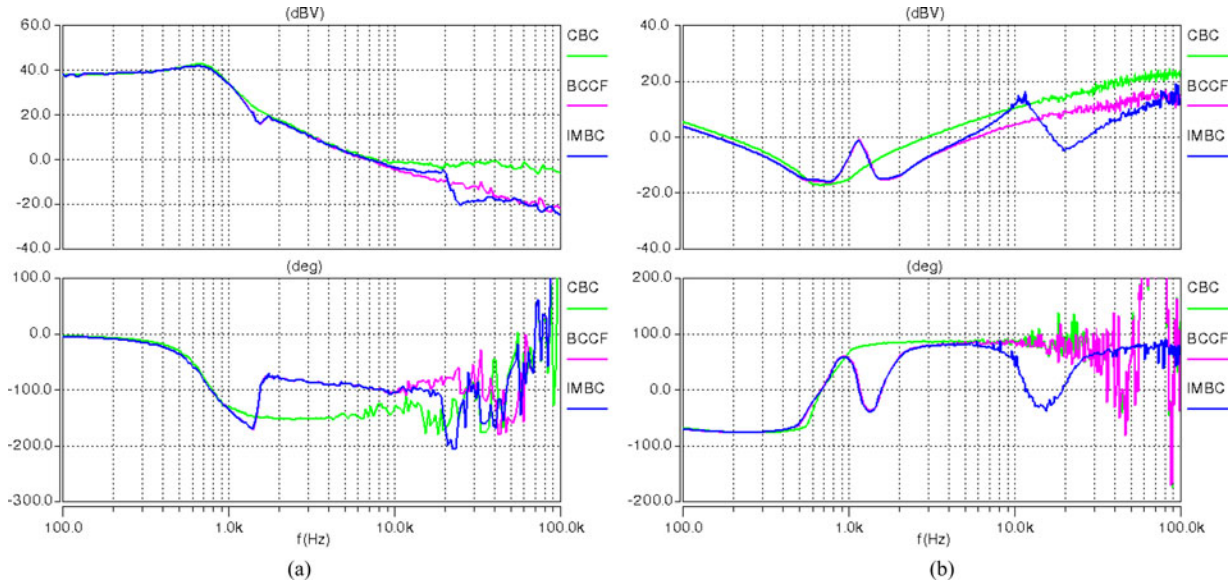

Fig. 7. Open-loop Bode plots of three converters. (a) Control-to-output frequency response. (b) Input impedance frequency response.

The open-loop frequency response Bode plots of the CBC, BCCF, and the proposed IMBC are shown in Fig. 7(a). The Bode plots indicated that the open-loop gain crossover frequencies of three converters are 6.92, 6.87, and 6.88 kHz. Meanwhile, the phase margins of three converters are, respectively, 54.4°, 83.1° and 82.7.1°. It proves that the open-loop dynamic characteristics of the BCCF and the proposed IMBC are exactly the same due to the same dominant roots. However, the curve of the proposed IMBC shows other resonant behaviors around 16 kHz cause by the extra zeros and poles after adding the ripple cancellation network. Overall, although the proposed IMBC is a sixth-order system, its open-loop frequency response curve is similar to that of a simple second-order conventional buck converter. The open-loop input impedance is one of the decisive factors describing the effect of the source interactions in a converter and the open-loop input impedance Bode plots of all the three converters are shown in Fig. 7(b). The Bode plots indicated that the BCCF and proposed IMBC are obviously the same at low frequencies because of their same main power parameters, likewise, the proposed IMBC shows extra resonant behaviors around 16 kHz cause by the ripple cancellation network.

Obviously, it seems that the sixth-order transfer function makes the proposed IMBC too difficult to control. However, the adding of the lossless ripple cancellation network only shows an extra resonant behavior around the *LC* resonance frequency in the open-loop frequency response Bode plots. The small-signal analysis and the Bode plots show that the proposed IMBC and the BCCF have very similar open-loop frequency characteristic, and also means the proposed IMBC shares the same close-loop control compensation design with the BCCF.

IV. Experimental Verifications

In order to verify the effectiveness of the IMBC, three 500 W prototypes are built and tested. The specifications of the tested converters are listed in Table I. The devices and instruments in the test experiment can be found in Table II.

TABLE II
Devices and Instruments in the Test Experiment

Category	Specification
Oscilloscope	Tektronix TDS 3034C
Input Source	TopCon DC power supply
MOSFET	IR IRFP90N20D
Output Diode	Motorola MUR3020WT
Magnetic Core	Arnold MS-141125-2
Output Capacitor	Nichicon 470μF200V
Buffer Capacitor	Fairchild 100V106 CBB
Ripple Capacitor	Sanyo 100μF100V

The weight analysis of three converters under the same power level has been listed in Table III. Although the weight of the proposed IMBC increased 22.1 g compared with the CBC, the integrated current ripple cancellation and RHP zero elimination functions still strengthen the advantage in power density since no extra filter is needed. The mass power ratio mass specific powers of three converters are respectively 135.5, 149.9, and 157.6 g.

Base on the power level of the proposed IMBC, an Arnold MS-141125-2 sendust powder core has been selected. The chosen core has many advantages such as cost-effective low loss material, operating frequencies to megahertz and no thermal aging. The winding arrangement and core parameters of the proposed IMBC have been given in Fig. 8. In order to achieve the designated coupling coefficient, the windings of the input and output inductors were twined on the both sides of the core. Meanwhile, the winding of the network entwined with both input and output windings to adjust the corresponding coupling coefficients.

TABLE III
SUMMARY OF WEIGHT FOR THREE CONVERTERS

Weight	CBC	BCCF	IMBC
Wire L_A (g)	4.8	4.8	4.8
Wire L_C (g)	—	12.1	12.1
Wire L_B (g)	—	—	2.0
Core (g)	35.0	35.0	35.0
C_b (g)	—	2.3	2.3
C_r (g)	—	—	5.7
C_o (g)	32.9	32.9	32.9
MOSFET (g)	5.6	5.6	5.6
Diode (g)	4.5	4.5	4.5
Control (g)	21.5	21.5	21.5
PCB (g)	14.7	14.7	14.7
Heat Sink (g)	16.5	16.5	16.5
Total (g)	**135.5**	**149.9**	**157.6**

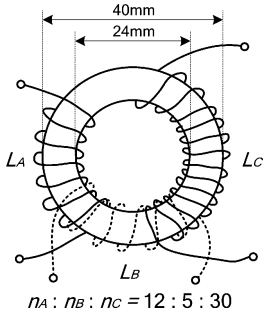

Fig. 8. Winding arrangement of the proposed IMBC.

The experimental results of the CBC, the BCCF, and the proposed IMBC under 250 W half load are shown in Fig. 9. The duty cycle of each converter is about 0.3 with the output voltage equal to 50 V. The input current ripples of the aforementioned converters are 2.1 A, 4 A, and 200 mA, respectively. Therefore, the proposed IMBC is able to minimize the input current ripple under the same load condition.

The comparison of the input current and output current waveforms of all three converters under 250 W half load is given in Fig. 10. As shown in the figures, the discontinuous-conduction-mode output current of the CBC will deteriorate the EMI problem and increase the output voltage ripple. In this case, the magnetic coupling of the input and output inductor seems to be the prefect solution to the problem. Although the BCCF decreases the output current ripple, the input current ripple almost doubled. As seen from three figures, after using the integrated magnetic technique, the proposed IMBC can minimize both the input current and output current without introducing any potential problem. The auxiliary current of the input current ripple cancellation branch in the IMBC is also shown in Fig. 10(c).

The input current and the buffer capacitor voltage waveforms of the proposed IMBC are presented in Fig. 11. As previously analyzed, the voltage of the buffer capacitor kept decreasing in the entire switching period with the average value equal to

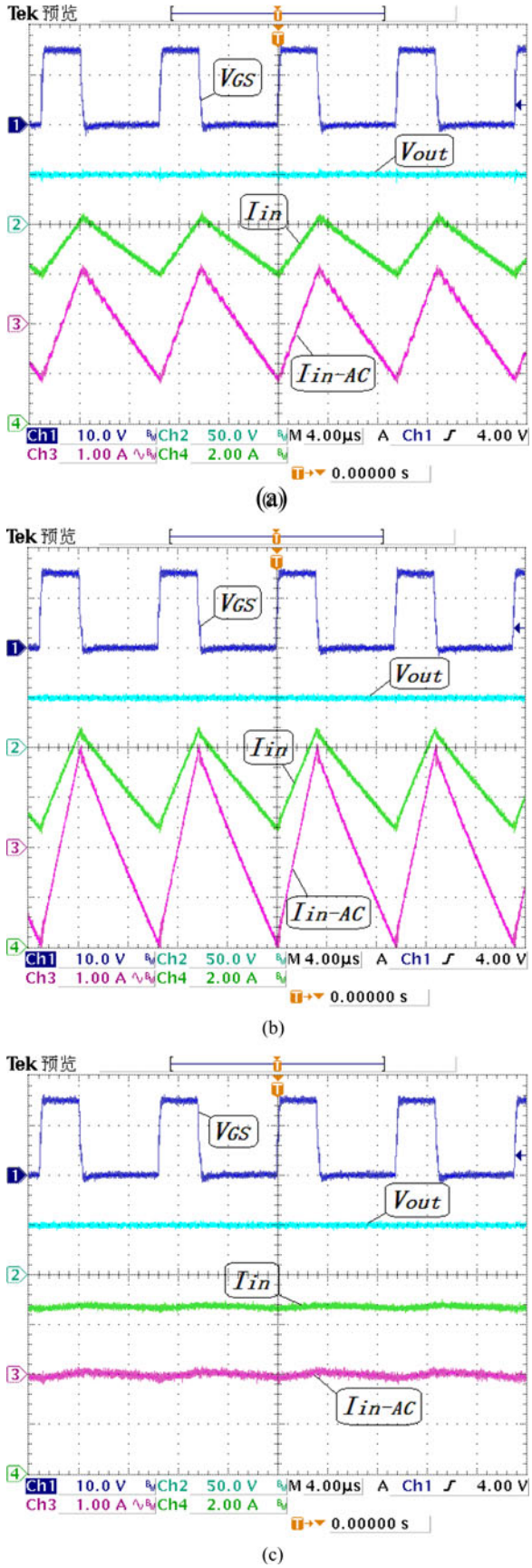

Fig. 9. Input current ripples of all three converters. (a) CBC. (b) BCCF. (c) IMBC.

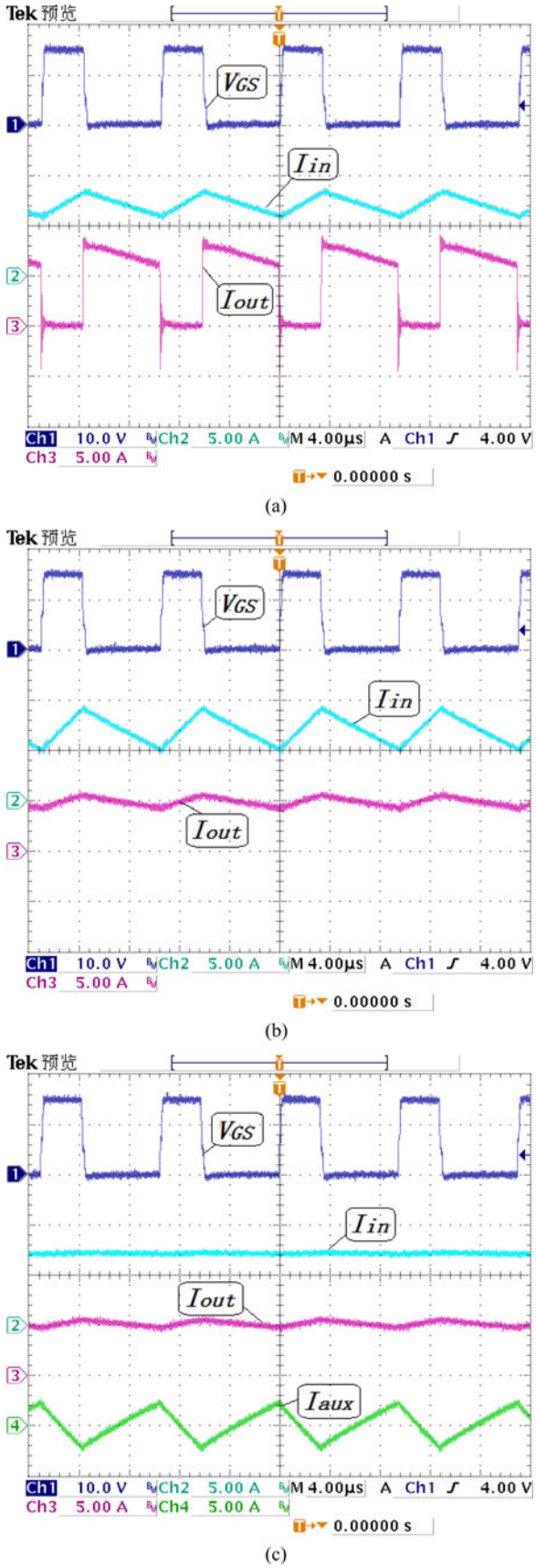

Fig. 10. Input and output current waveforms of all three converters. (a) CBC. (b) BCCF. (c) IMBC.

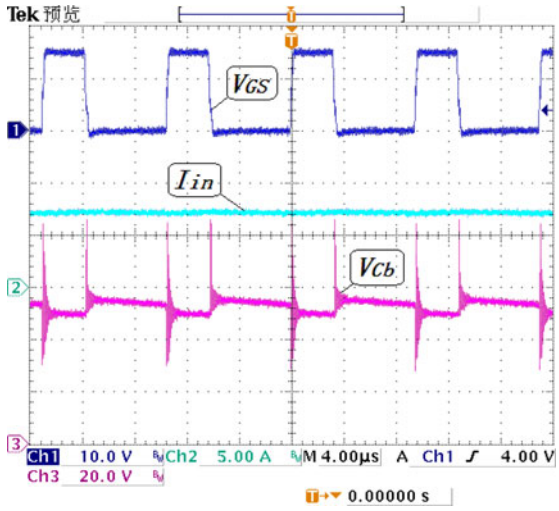

Fig. 11. Input current and buffer capacitor voltage waveforms of the proposed IMBC.

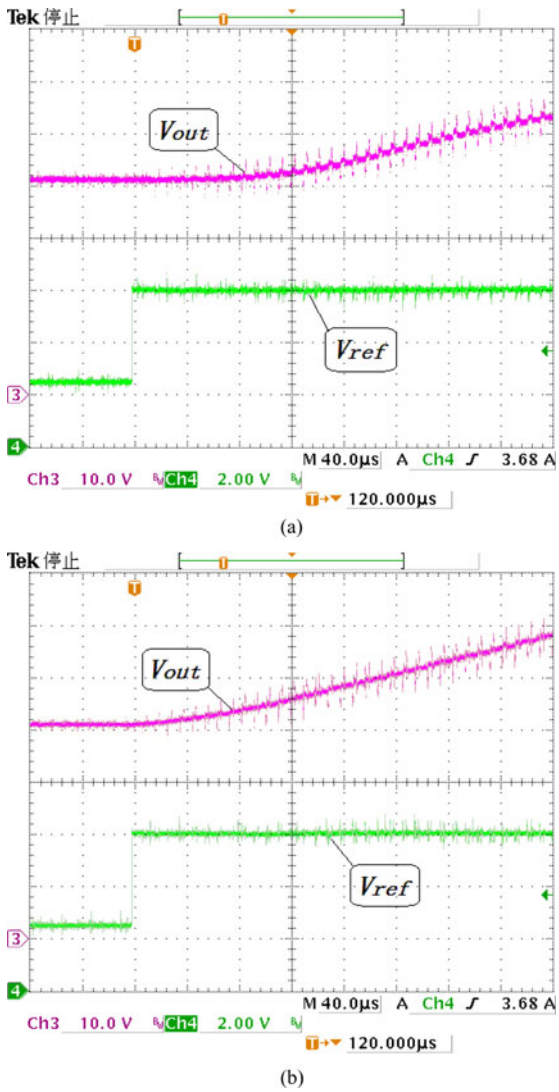

Fig. 12. Open-loop output voltage waveforms of the converters under the step change duty cycle. (a) CBC. (b) IMBC.

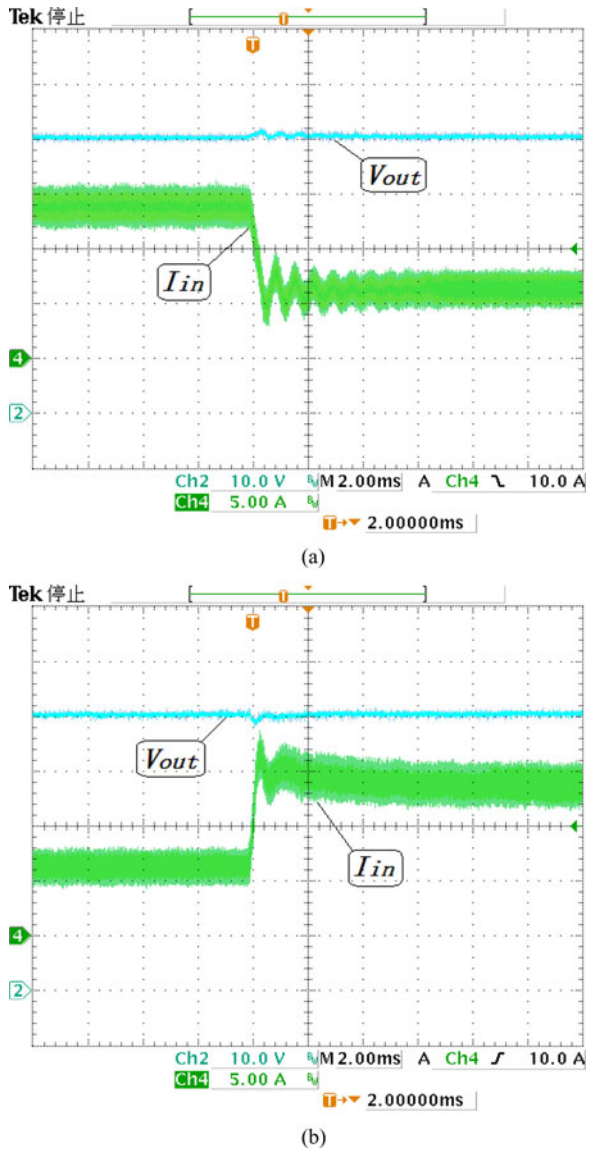

Fig. 13. Experimental output voltage and input current results of the BCCF. (a) From full load to half load. (b) From half load to full load.

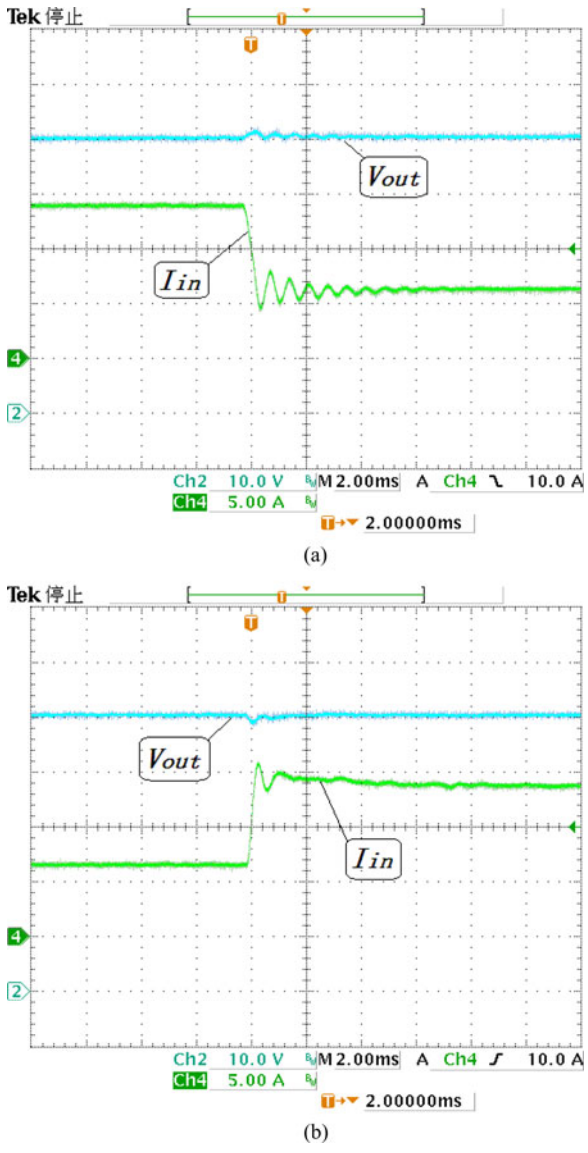

Fig. 14. Experimental output voltage and input current results of the proposed IMBC. (a) From full load to half load. (b) From half load to full load.

the output voltage. At the moment that the main switch turned OFF, the energy stored in the input inductor L_A starts to transfer through the output diode D. However, due to the prescribed coupled direction between L_A and L_C, the current of output inductor L_C starts to decrease. For that reason, part of the energy has been stuck between the diode and the output inductor, causing the voltage of the buffer capacitor to increase rapidly. When the switch turns ON, the buffer capacitor voltage drops rapidly because the energy stored in the buffer capacitor has been transferred to the load to eliminate the RHP zero. As a result, the buffer capacitor can be seen as an energy buffer in order to provide a stable energy to the load during the power diode off state.

The open-loop output voltage waveforms of the CBC and proposed IMBC under the same step change duty ratio from 0.15 to 0.6 are shown in Fig. 12 to verify the elimination of the RHP zero. Due to the effect of the RHP zero, the output voltage of the CBC maintains the original voltage (around 42 V as $D = 0.15$) almost 100 μs (ten switching period) after the step signal arrives. By contrast, the output voltage of the proposed IMBC rises up as soon as the step change in the signal happens since no previous RHP zero exists. Because both CBC and proposed IMBC have the same equivalent input inductor, the rising slopes of both converters are almost the same when steady rise process arrived. The comparison experimental result proves that the proposed IMBC has better dynamic response under the step changing signal, which also means the proposed IMBC has the ability to realize higher close-loop bandwidth.

The experimental output voltage $V_{\rm out}$ and the input current $I_{\rm in}$ waveforms of the BCCF and the proposed IMBC changing from 500 W full load to 250 W half load and changing from 250 W half load to 500 W full load under same PI closed-loop

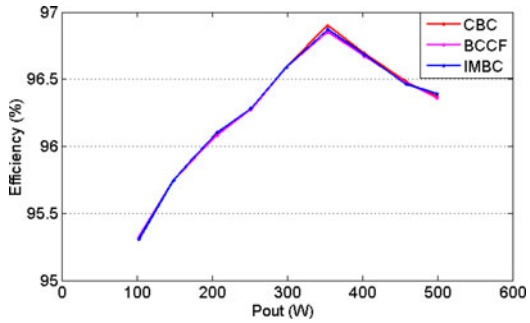

Fig. 15. Efficiency curves of three converters.

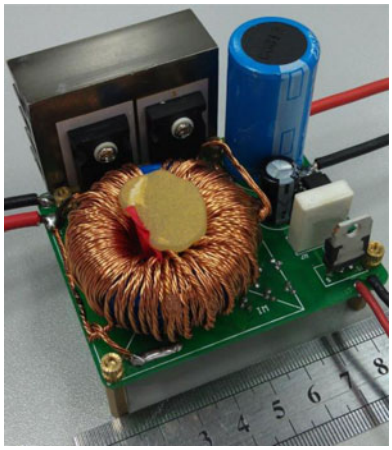

Fig. 16. Photograph of the proposed IMBC.

control are given respectively in Figs. 13 and 14. The transient voltage ripple is relatively small and the transient time less than 6 ms. The figures not only show the proposed IMBC with an excellent closed-loop control, but also prove that both BCCF and IMBC have the same dynamic characteristics.

The measured efficiencies of the CBC, BCCF, and proposed IMBC at different loads are given in Fig. 15. As shown in the figure, the maximum efficiency points of all the three converters appear around 350 W are respectively 96.91%, 96.85%, and 96.87% with the conversion of 36-V input to 50-V output operating at 100 kHz switching frequency. As the load increases, the efficiencies of all three converters start to decrease. By comparing the efficiency curves, three converters have the similar efficiencies in all power range. However, the BCCF and proposed IMBC seem to have lower efficiencies (around 0.05%, 0.25 W) than the CBC, because the adding of the output inductor winding introduce an extra series resistance. Since the coupled *LC* filter and the ripple cancellation network are essentially lossless circuits, the small power losses cause by these structure can be ignored in high-power applications.

The photograph of the test IMBC prototype is shown in Fig. 16. The size of the proposed IMBC is 76 mm $\times$ 61 mm $\times$ 40 mm. In general, the size of the passive components can be reduced to reach higher power density if higher switching frequency was selected.

V. Conclusion

An integrated magnetic boost converter with input and output current ripple cancellation and RHP zero elimination has been proposed in this paper. The relevant equations for the design procedure, the operation principle, and the main theoretical waveforms are discussed in detail. The main advantages of the proposed converter include input and output current ripple cancellation and RHP zero elimination, both advantages are very important especially in high power fast dynamic response applications.

Experimental results obtained from a 500 W prototype have validated the concept. The input current ripple dropped to one-twelfth of the original in CBC, and the output current worked in continuous-conduction-mode with a small ripple. Meanwhile, the integrated magnetic technique in the proposed IMBC was able to eliminate the RHP zero of the CBC in order to reach higher close-loop bandwidth, and the maximum efficiency of the prototype ran up to 96.8%. Compared with the CBC and BCCF, the proposed integrated magnetic boost converter shows significant advantages due to the distinctive integrated magnetic technique.

References

[1] G. W. Wester and R. D. Middlebrook, "Low-frequency characterization of switched dc-to-dc converters," in *Proc. IEEE Power Electronics. Spec. Conf.*, 1972, pp. 9–20.

[2] J. Sun, D. M. Mitchell, M. F. Greuel, P. T. Krein, and R. M. Bass, "Averaged modeling of PWM converters operating in discontinuous conduction mode," *IEEE Trans. Power Electron.*, vol. 16, no. 4, pp. 482–492, Jul. 2001.

[3] E. Van Dijk, J. N. Spruijt, D. M. O'Sullivan, and J. B. Klaassens, "PWM switch modeling of DC–DC converters," *IEEE Trans. Power Electron.*, vol. 10, no. 6, pp. 659–665, Nov. 1995.

[4] K. Viswanathan, R. Oruganti, and D. Srinivasan, "A novel tri-state boost converter with fast dynamics," *IEEE Trans. Power Electron.*, vol. 17, no. 5, pp. 677–683, Sep. 2002.

[5] A. Burak, "An Improved ZVT–ZCT PWM DC–DC Boost Converter with Increased Efficiency," *IEEE Trans. Power Electron.*, vol. 29, no. 4, pp. 1919–1926, Apr. 2014.

[6] K. Viswanathan, R. Oruganti, and D. Srinivasan, "Dual-mode control of tri-state boost converter for improved performance," *IEEE Trans. Power Electron.*, vol. 20, no. 4, pp. 790–797, Jul. 2005.

[7] J. Calvente, L. Martinez-Salamero, H. Valderrama, and E. Vidal Idiarte, "Using magnetic coupling to eliminate right half-plane zeros in boost converters," *IEEE Trans. Power Electron. Lett.*, vol. 2, no. 2, pp. 58–62, Jun. 2004.

[8] P. Rueda, S. Ghani, and P. Perol, "A new energy transfer principle to achieve a minimum phase & continuous current boost converter," in *Proc. IEEE Power Electronics. Spec. Conf.*, Jun. 2004, vol. 3, pp. 2232–2236.

[9] R. Erickson and D. Maksimovic, *Fundamentals of Power Electronics*, 2nd ed. USA: Kluwer Academic Publishers, 2001, pp. 42–45.

[10] S. Maniktala, *Switching Power Supplies A to Z[M].* New York, NY, USA: Elsevier, 2006, pp. 51–54.

[11] D. C. Hamill and P. T. Krein, "A 'zero' ripple technique applicable to any dc converter," in *Proc. IEEE Power Electronics. Spec. Conf.*, 1999, vol. 2, pp. 1165–1171.

[12] P. W. Lee, Y. S. Lee, D. K. Cheng, and X. C. Liu, "Steady-state analysis of an interleaved boost converter with coupled inductors," *IEEE Trans. Ind. Electron.*, vol. 47, no. 4, pp. 787–795, Aug. 2000.

[13] H. L. Do, "Improved ZVS DC-DC converter with a high voltage gain and a ripple-free input current," *IEEE Trans. Circuits Syst. I, Reg. Papers*, vol. 59, no. 4, pp. 846–853, Apr. 2012.

[14] N. K. Poon, J. C. P. Liu, C. K. Tse, and M. H. Pong, "Techniques for input ripple current cancellation: Classification and implementation," *IEEE Trans. Power Electron.*, vol. 15, no. 6, pp. 1144–1152, Nov. 2000.

[15] F. Musavi, M. Edington, W. Eberle, and W. G. Dunford, "Control loop design for a PFC boost converter with ripple steering," *IEEE Trans. Ind. Appl.*, vol. 49, no. 1, pp. 118–126, Jan./Feb. 2013.
[16] J. Wang, W. G. Dunford, and K. Mauch, "Analysis of a ripple-free input current boost converter with discontinuous conduction characteristics," *IEEE Trans. Power Electron.*, vol. 12, no. 4, pp. 684–694, Jul. 1997.
[17] R. Martinelli and C. Ashley, "Coupled inductor boost converter with input and output ripple cancellation," in *Proc. IEEE Appl. Power Electron. Conf.*, 1991, pp. 567–572.
[18] D. Diaz, D. Meneses, J. A. Oliver, O. Garcia, P. Alou, and J. A. Cobos, "Dynamic analysis of a boost converter with ripple cancellation network by model-reduction techniques," *IEEE Trans. Power Electron.*, vol. 24, no. 12, pp. 2769–2775, Dec. 2009.
[19] Y. Jang and M. Jovanovic, "New two-inductor boost converter with auxiliary transformer," *IEEE Trans. Power Electron.*, vol. 19, no. 1, pp. 169–175, Dec. 2004.
[20] Q. Li and P. Wolfs, "A current fed two-inductor boost converter with an integrated magnetic structure and passive lossless snubbers for photovoltaic module integrated converter applications," *IEEE Trans. Power Electron.*, vol. 22, no. 1, pp. 309–321, Jan. 2007.
[21] Q. Li and P. Wolfs, "An analysis of the ZVS two-inductor boost converter under variable frequency operation," *IEEE Trans. Power Electron.*, vol. 22, no. 1, pp. 120–131, Jan. 2007.
[22] C. Quinn, K. Rinne, T O'Donnell, M. Duffy, and C. O. Mathuna, "A review of planar magnetic techniques and technologies," in *Proc. IEEE Appl. Power Electron. Conf.*, 2001, vol. 2, pp. 1175–1181.
[23] J. M. Lopera, J. Prieto, A. M. Pernia, F. Nuno, M. J. M. De Graaf, J. W. Waandaers, and L. A. Barcia, "Design of integrated magnetic elements using thick-film technology," *IEEE Trans. Power Electron.*, vol. 14, no. 3, pp. 408–414, May. 1999.
[24] J. Sun, K. F. Webb, and V. Mehrotra, "Integrated magnetics for current-doubler rectifiers," *IEEE Trans. Power Electron.*, vol. 19, no. 3, pp. 582–590, May. 2004.
[25] J. Sun and V. Mehrotra, "Orthogonal winding structures and design for planar integrated magnetics," *IEEE Trans. Ind. Electron.*, vol. 55, no. 3, pp. 1463–1469, Mar. 2008.
[26] L. Yan and B. Lehman, "An integrated magnetic isolated two-inductor boost converter: Analysis, design, and experimentation," *IEEE Trans. Power Electron.*, vol. 20, no. 2, pp. 332–342, Mar. 2005.
[27] K. Jin, Y. Sun, M. Xu, D. Sterk, and F. C. Lee, "Integrated magnetic self-driven ZVS nonisolated full-bridge converter," *IEEE Trans. Ind. Electron.*, vol. 57, no. 5, pp. 1615–1623, May 2010.
[28] P. Xu, Y. Mao, P. L. Wong, and F. C. Lee, "Design of 48 V voltage regulator modules with a novel integrated magnetics," *IEEE Trans. Power Electron.*, vol. 17, no. 6, pp. 990–998, Nov. 2002.
[29] Q. Li and P. Wolfs, "A leakage-inductance-based ZVS two-inductor boost converter with integrated magnetics," *IEEE Power Electron. Lett.*, vol. 3, no. 2, pp. 67–71, Jun. 2005.
[30] X. L. Gao and A. R , "A novel buck-cascaded two-inductor boost converter with integrated magnetics," in *Proc. Int. Telecommun. Energy Conf.*, 2004, pp. 190–197.
[31] R. T. Chen and Y. Y. Chen, "A novel single stage push pull converter with integrated magnetics and ripple-free input current," in *Proc. IEEE Power Electron. Spec. Conf.*, 2004, vol. 5, pp. 3848–3853.

Yu Gu (S'12) was born in Shenzhen, China, in 1986. He received the B.S. degree from South China University of Technology, Guangzhou, China, in 2009, and the M.S. degree from the Harbin Institute of Technology Shenzhen Graduate School, China, in 2011, where he is currently working toward the Ph.D. degree in power electronics and power drives.

His research interests include power electronics, renewable energy systems, multilevel power converters and pulse-width modulation techniques.

Donglai Zhang (M'03) was born in Jilin, China, in 1973. He received the B.S., M.S., and Ph.D. degrees from the Harbin Institute of Technology, Harbin, China, in 1994, 1996, 1999, respectively.

Since 2005, he has been a Professor at the Harbin Institute of Technology Shenzhen Graduate School. His research interests include analysis, modeling and control of power converters, digital control techniques for power electronic circuits, and grid-connected converters for renewable energy systems. In these research fields, he was leading several industrial and government projects.

Dr. Zhang is a Member of the China Power Electronics Society.

Zhongyang Zhao was born in Harbin, China, in 1990. He received the B.S. degree from the Harbin Institute of Technology, Harbin, China, in 2012, and he is currently working toward the M.S. degree in power electronics and power drives in Harbin Institute of Technology Shenzhen Graduate School, China.

His research interests include power converters for solar energy, particularly micro inverters for ac photovoltaic modules, and pulse-width modulation techniques.